

Imaging resident and recruited macrophage contribution to Wallerian degeneration

Alexandre Boissonnas, Floriane Louboutin, Marie Laviron, Pierre-Louis Loyher, Elodie Reboussin, Sandrine Barthélémy, Annabelle Réaux-Le Goazigo, Christian S. Lobsiger, Béhazine Combadière, Stéphane Melik Parsadaniantz, et al.

▶ **To cite this version:**

Alexandre Boissonnas, Floriane Louboutin, Marie Laviron, Pierre-Louis Loyher, Elodie Reboussin, et al.. Imaging resident and recruited macrophage contribution to Wallerian degeneration. Journal of Experimental Medicine, 2020, 217 (11), 10.1084/jem.20200471 . hal-03047020

HAL Id: hal-03047020
https://hal.sorbonne-universite.fr/hal-03047020

Submitted on 8 Dec 2020

HAL is a multi-disciplinary open access archive for the deposit and dissemination of scientific research documents, whether they are published or not. The documents may come from teaching and research institutions in France or abroad, or from public or private research centers.

L'archive ouverte pluridisciplinaire **HAL**, est destinée au dépôt et à la diffusion de documents scientifiques de niveau recherche, publiés ou non, émanant des établissements d'enseignement et de recherche français ou étrangers, des laboratoires publics ou privés.

JEM Journal of Experimental Medicine

BRIEF DEFINITIVE REPORT

Imaging resident and recruited macrophage contribution to Wallerian degeneration

Alexandre Boissonnas[1], Floriane Louboutin[1], Marie Laviron[1], Pierre-Louis Loyher[2], Elodie Reboussin[3], Sandrine Barthelemy[1], Annabelle Réaux-Le Goazigo[3], Christian S. Lobsiger[4], Béhazine Combadière[1], Stéphane Mélik Parsadaniantz[3]*, and Christophe Combadière[1]*

Wallerian degeneration (WD) is a process of autonomous distal degeneration of axons upon injury. Macrophages (MPs) of the peripheral nervous system (PNS) are the main cellular agent controlling this process. Some evidence suggests that resident PNS-MPs along with MPs of hematogenous origin may be involved, but whether these two subsets exert distinct functions is unknown. Combining MP-designed fluorescent reporter mice and coherent anti–Stokes Raman scattering (CARS) imaging of the sciatic nerve, we deciphered the spatiotemporal choreography of resident and recently recruited MPs after injury and unveiled distinct functions of these subsets, with recruited MPs being responsible for efficient myelin stripping and clearance and resident MPs being involved in axonal regrowth. This work provides clues to tackle selectively cellular processes involved in neurodegenerative diseases.

Introduction

Peripheral nervous system (PNS) reparation after trauma is crucial for survival of complex organisms. Following nerve injury, axons undergo a process of autonomous distal degeneration termed Wallerian degeneration (WD; Coleman and Freeman, 2010; Tricaud and Park, 2017). Because of the loss of contact between Schwann cells and neuronal fibers in the PNS, the myelin sheath disintegrates, and the proper clearance of the myelin debris is required to complete nerve regeneration (Stassart et al., 2013). Macrophages (MPs) in the PNS are believed to be the main cellular agent responsible for myelin clearance (Klein and Martini, 2016; Martini et al., 2008) and are suspected to participate in axon regeneration with Schwann cells by creating a growth-permissive environment (Chen et al., 2015; DeFrancesco-Lisowitz et al., 2015). For a long time, the main proposed models suggested that PNS-MPs during WD mainly arise from CCR2-mediated recruitment and differentiation of monocytes (Mo's), which progressively switch from an M1-like profile, exerting phagocytic-mediated myelin clearance, toward a M2-like polarization profile, participating in axon regeneration (Chen et al., 2015).

There is evidence now that resident MPs are directly involved in the process of WD along with hematogenous inflammatory Mo-derived (MoD) MPs, but their respective implication and the spatiotemporal dynamics of their actions are unclear due to the difficulty to discriminate between them, as they likely exert overlapping functions. Tissue-resident MPs in mice, such as alveolar MPs, Kupffer cells, or microglia (Ginhoux and Jung, 2014; Gomez Perdiguero et al., 2015), can have an embryonic origin and self-renew with minimal to no replacement by Mo from adult hematopoiesis. Some others have a hematopoietic stem cell origin, harboring a long-term survival with slow turnover rates such as lung interstitial MP (Chakarov et al., 2019; Gibbings et al., 2017; Rodero et al., 2015) or cardiac MP (Epelman et al., 2014; Molawi et al., 2014) or a fast turnover rate such as intestinal MP (Bain et al., 2014). The origin of PNS-MPs is still unclear (Kolter et al., 2020). Irradiated bone marrow chimeric models support a global turnover of this subset from blood Mo's (Vass et al., 1993). Although irradiation is known to favor resident MP replacement by MoD cells, a significant fraction the former still persist, arguing for a long-term resident PNS-MP population (Müller et al., 2010). This subset has been demonstrated to proliferate upon nerve injury and participate in the process of WD along with MPs of hematogenous origin (Mueller et al., 2003). Ydens et al. (2020) have recently investigated this question and identified that MPs in the sciatic nerve arise from late embryonic precursors progressively replaced by MPs of adult Mo origin. Based on single-cell RNA sequencing (RNA-seq), they uncovered that endoneurial and epineurial MPs

[1]Sorbonne Université, INSERM, CNRS, Centre d'Immunologie et des Maladies Infectieuses Cimi-Paris, Paris, France; [2]Immunology Program, Sloan Kettering Institute, Memorial Sloan Kettering Cancer Center, New York, NY; [3]Department Therapeutique, Institut de la Vision, INSERM UMR S 968, CNRS UMR 7210, Sorbonne Université, Paris, France; [4]Institut du Cerveau et de la Moelle épinière, ICM, INSERM U 1127, CNRS UMR 7225, Sorbonne Université, Paris, France.

*S. Mélik Parsadaniantz and C. Combadière contributed equally to this paper; Correspondence to Alexandre Boissonnas: alexandre.boissonnas@upmc.fr.

© 2020 Boissonnas et al. This article is distributed under the terms of an Attribution–Noncommercial–Share Alike–No Mirror Sites license for the first six months after the publication date (see http://www.rupress.org/terms/). After six months it is available under a Creative Commons License (Attribution–Noncommercial–Share Alike 4.0 International license, as described at https://creativecommons.org/licenses/by-nc-sa/4.0/).

Downloaded from http://rupress.org/jem/article-pdf/217/11/e20200471/1047202/jem_20200471.pdf by Curie Bib Paris user on 08 December 2020

harbor distinct transcriptomic signatures specific for the sciatic nerve. Beyond the characterization of their various ontogeny, the relative contribution of resident MPs and inflammatory MoD-MP during WD is unknown. Our study combines murine models with MP-designed fluorescent reporters and coherent anti–Stokes Raman scattering (CARS) imaging of the PNS (Bélanger et al., 2011; Lee and Serrels, 2016) to track the dynamics of MoD-MP and resident MP amplification and distribution in the sciatic nerve over time following chronic constriction injury (CCI).

Results and discussion

Two distinct MP subsets accumulate in injured sciatic nerve

CARS imaging is a nonlinear optical imaging process allowing chemically specific label-free structural imaging from live tissue at the cellular level by enhancing the weak spontaneous Raman scattering given by the nuclear vibration of molecular bonds (Le et al., 2010; Lee and Serrels, 2016). We monitored the process of WD in the sciatic nerve over time following CCI, tuning our multiphoton imaging system to generate a CARS signal from the CH_2 stretching mode at 2,925 cm^{-1}, allowing the visualization of lipid-rich structures such as the myelin sheath in freshly isolated sciatic nerves (Fig. S1 a). Morphological changes in the myelin sheath were quantified and qualified over 2 mo to visualize the sequential phases of WD in the vicinity of the constriction areas (Fig. 1, a and b). We defined a demyelination phase characterized by a rapid myelin breakdown within the first 10 d with consequent myelin degeneration lasting ∼3 wk. The remyelination phase started subsequently and was characterized by progressive recovery of the myelin sheath lasting ≥2 mo from the time of injury. Inflammatory Mo's (defined as $CD45^+$ $CD11b^+$ $Ly6G^-$ $Ly6C^+$) and MPs (defined as $CD45^+$ $CD11b^+$ $Ly6G^-$ $Ly6C^-$ $CD64^+$) were quantified over time by flow cytometry in sciatic nerves of C57BL6 mice as defined by the gating strategy (Fig. S1, b and c). At steady state, $Ly6C^{high}$-Mo's were almost absent from the nerve (Fig. 1 c, left panel), and the number of MPs harvested was very low (12 ± 7 cells/mg; Fig. 1 c, middle panel). $Ly6C^{high}$-Mo's infiltrated within 12 h following nerve injury, rapidly followed by MPs peaking between 5 and 10 d during the demyelination phase, with an increasing proportion expressing MHC class II over time (Fig. 1 c, right panel). Both subsets contracted during the regeneration phase, being barely detectable by flow cytometry after 2 mo (Fig. 1 c).

We next performed multiphoton imaging of freshly explanted sciatic nerve using the MacBlue × *Cx3cr1*$^{egfp/+}$ transgenic mouse model (Loyher et al., 2018; Rodero et al., 2015) to identify Mo and MP localization based on the expression of enhanced GFP (EGFP) and enhanced CFP (ECFP) in combination with CARS imaging. The *Csf1r* promoter in MacBlue mice lacks the 150-bp trophoblast- and osteoclast-specific transcription start sites driving the expression of ECFP on MoD cells and a fraction of granulocytes, but the expression of this reporter is absent on the majority of tissue-resident MP subsets, except for alveolar MPs, microglia, and Langerhans cells (Loyher et al., 2018; Sauter et al., 2014). Microglial cells are reported to express high levels of EGFP in the *Cx3cr1*$^{egfp/+}$ mouse (Jung et al., 2000) as well as PNS-MPs (Kolter et al., 2019, 2020), but the relative expression of ECFP and EGFP in MPs of the PNS has never been studied. In contralateral nerves representative of noninjured nerves (control nerves), only a few $EGFP^+$ cells and no $ECFP^+$ cells were detected. These cells, located at the epi- and perineurium, displayed a stellar and elongated shape when located at the endoneurium in close contact with nerve fibers as reported by Ydens et al. (2020) and in other tissue-associated nerves (Kolter et al., 2020). Flow cytometry analysis confirmed that resident MPs express EGFP, but not ECFP, arguing for the recent recruitment of $ECFP^+$ cells (Fig. 1 e). In injured nerves, 10 d after CCI, $ECFP^+$ cells densely aggregated near the constricted area around the epineurium as well as in direct contact with the myelinated fibers, while only a few $EGFP^+$ cells were still detectable (Fig. 1 d). Although the channel for ECFP detection was color-coded in dark blue like second harmonic generation (SHG), ECFP-expressing cells appear in cyan due to spectral overlap between ECFP and EGFP and because this subset might coexpress the EGFP reporter. Flow cytometry with proper fluorescent compensations confirmed that $ECFP^+$ cells also coexpress EGFP fluorescence at a level lower or similar to the one expressing only EGFP (Fig. 1 e, left panels). We chose to simplify the nomenclature and defined the $ECFP^+$ $EGFP^+$ subset as $ECFP^+$ cells and the $ECFP^-$ $EGFP^+$ subsets as $EGFP^+$ cells. $ECFP^+$ cells are composed of $Ly6C^{high}$-Mo's as well as $Ly6C^{low}$ $CD64^+$ MPs (previously named "Mono-Mac waterfall"; Ydens et al., 2020), while $EGFP^+$ cells represent exclusively $Ly6C^{low}$ $CD64^+$ MPs and accumulate by 10 d after injury (Fig. 1 e, right panels). Hence, we hypothesized that $ECFP^+$ cells represent the recently recruited Mono-Mac waterfall, while $EGFP^+$ cells could be resident MPs activated after nerve injury.

MP subsets accumulate in the nerve in two consecutive waves with distinct transcriptomic signatures

We further investigated the kinetics and distribution of $ECFP^+$ and $EGFP^+$ cell infiltration on nerve cryosections (Fig. 2 a). $ECFP^+$ cells accumulated along the fibers during the demyelination phase (5–10 d after injury) and progressively disappeared during the remyelination phase (20–60 d after injury), while the number of $EGFP^+$ cells increased by day 10 and peaked at day 30, representing the dominant subset, and disappeared as well afterward (Fig. 2 b). Quantification of their relative distance to the constricted areas of the nerve showed that the majority of $ECFP^+$ cells (Fig. S2, a and b, left panel) were distributed in the vicinity of the constriction 5 d after injury and that they progressively accumulate further and further away from the constriction by day 10 and reduced in number thereafter. $EGFP^+$ cells also preferentially accumulated close to the constriction by day 10 but further accumulated at distance from the constriction after 30 d, confirming spatial and temporal desynchronization of the two subsets (Fig. S2, a and b, right panel). $ECFP^+$ and $EGFP^+$ cells displayed a strikingly different morphology (Fig. 2 c), with higher expression of CCR2, MHC class II, and the scavenger receptor CD206, but not CD36, on the former (Fig. S2 c). Comparative RNA-seq analysis between $ECFP^+$ and $EGFP^+$ sorted MPs showed different transcriptomic profiles with notably hierarchical clustering of 124 differentially regulated genes,

Downloaded from http://rupress.org/jem/article-pdf/217/11/e20200471/1047202/jem_20200471.pdf by Curie Bib Paris user on 08 December 2020

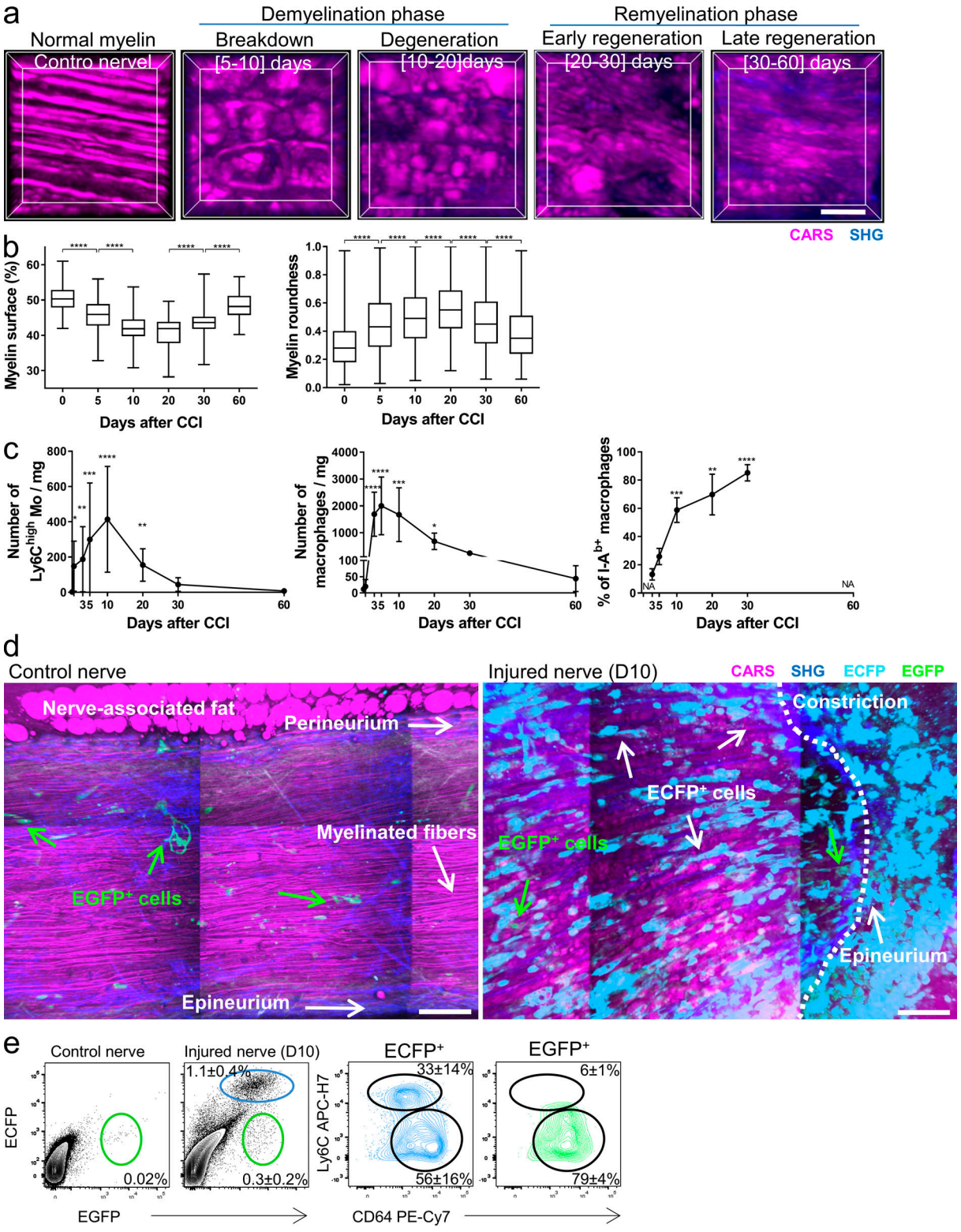


Figure 1. **Tracking MP infiltration during WD of the sciatic nerve using CARS imaging. (a)** TPLSM 3D images of intact sciatic nerve after CCI show representative structures of the myelin sheath over time after injury, defining the progressive steps of the WD. Scale bar = 15 µm. **(b)** Quantification of myelin degeneration based on CARS imaging (n = 3–4 mice for each time point, processed independently; one-way ANOVA with Bonferroni multiple comparison tests are indicated). **(c)** Kinetics of Mo and MP accumulation after injury; results represent mean ± 95% confidence interval (CI) of the absolute number of cells per milligram of nerve. (n = 6 mice for each time point; n = 12 for days 3 and 10; mice are pooled from two or three independent experiments, P values according to one-way ANOVA with Bonferroni multiple comparison to day 0 tests are indicated by asterisks). N/A, not applicable due to the low number of cells. **(d)** TPLSM tiled and stitched image reconstitution of noninjured, control (contralateral), and injured (ipsilateral) sciatic nerves from a MacBlue × *Cx3cr1*$^{egfp/+}$ mouse show the accumulation of Mo's and MPs in constricted areas 10 d after CCI. Scale bar = 70 µm. **(e)** Phenotypic characterization of EGFP$^+$ and ECFP$^+$ cells in sciatic nerves 10 d after CCI. Mean percentage ± SD for dot plots are indicated for each subset (n = 6 out of two experiments). See also Fig. S1. *, P < 0.05; **, P < 0.01; ***, P < 0.001; ****, P < 0.0001.

Downloaded from http://rupress.org/jem/article-pdf/217/11/e20200471/1047202/jem_20200471.pdf by Curie Bib Paris user on 08 December 2020

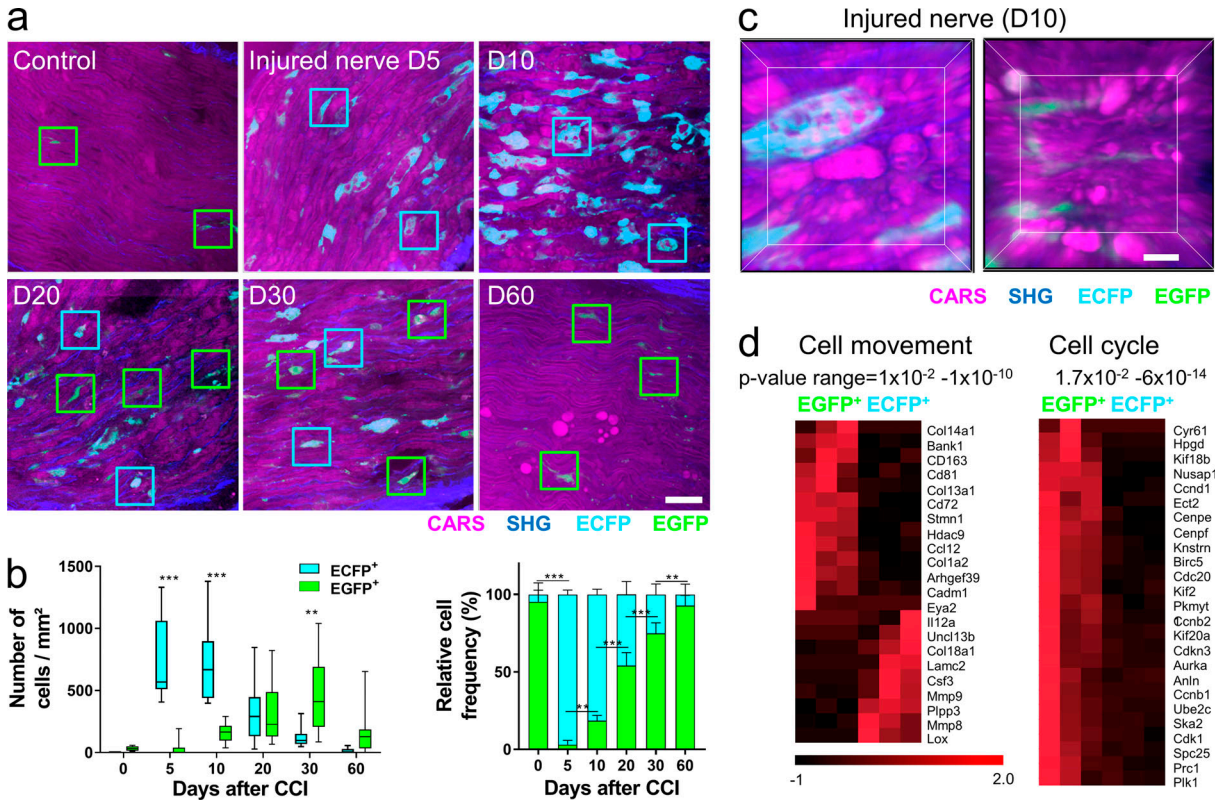


Figure 2. **Different MP subsets accumulate in sequential waves. (a)** TPLSM images of sciatic nerve cryosections of MacBlue × *Cx3cr1*$^{egfp/+}$ mice showing the kinetics of fluorescent cell accumulation following CCI. Images represent magnifications of a wider field of tiled and stitched images of the nerve sections at respective days after CCI, Scale bar = 30 µm. **(b)** Quantification (mean ± 95% CI) of the absolute number per square millimeter (left panel) and relative proportion of EGFP⁺ and ECFP⁺ cells (right panel) from cryosections (n = 4–5 mice per time point processed independently; P value of two-way ANOVA with Bonferroni multiple comparison tests are indicated). **(c)** 3D TPLSM images showing typical shapes of ECFP⁺ and EGFP⁺ cells in injured nerve. Scale bar = 10 µm. **(d)** Heatmaps of gene with significant differential expression between ECFP⁺ and EGFP⁺ MPs (fold change >2 with FDR <0.05) and specifically enriched in indicated functional clusters according to IPA (range P values for each functional cluster are indicated). Three independent RNA isolations were prepared from a pool of three mice each. See also Fig. S2. **, P < 0.01; ***, P < 0.001.

showing that these subsets are also functionally distinct (Fig. S2 d and Table S1). Among these genes, we identified significant enrichment of genes associated with cellular movement and cell cycle functional pathways according to Ingenuity Pathway Analysis (IPA; Fig. 2 f). These identified clusters suggested specific involvement of ECFP⁺ MPs in extracellular matrix (ECM) remodeling, with higher expression of *Lox*, *Lamc2*, and *MMP*-associated genes, and specific implication of EGFP⁺ MPs in ECM regeneration, with not only higher expression of different collagen-associated genes and *Cyr61* (involved in ECM formation) but also higher proliferative activity, with up-regulation of up to 25 genes enriched in cell cycle pathways. *Lyve1* and *Mgl2* were both enriched in the EGFP+ MP (Table S1). *Lyve1* is associated with vascular- (Lyve1^{high}MHCII^{low}) and nerve-associated (Lyve1^{low}MHCII^{high}) interstitial MPs in the lungs (Chakarov et al., 2019), and *Mgl2* is associated with endoneurial MPs after injury (Ydens et al., 2020). Out of these 124 genes, in accordance with the resident epineurial MPs signature (Ydens et al., 2020), *Retnla* and *Clec10a*, coding for Relmα and Mgl1, respectively, were both significantly enriched in the EGFP⁺-sorted MPs compared with ECFP⁺ MPs at a log fold change of 1.4 and 1.3, respectively. No inflammatory pathway–associated gene cluster was uncovered among these 124 genes, suggesting that either the two MP subsets evenly up-regulated inflammatory genes or that inflammation might already be dampened by day 14 in favor of the regenerative process. The latter is in accordance to the contraction phase observed on ECFP⁺ MP (Fig. 2 b). Still, *Ccl8*, *Ccl12*, and *Cxcl9* transcripts were enriched in EGFP⁺ MPs (Table S1), suggesting that they maintained active Mo chemoattraction at this time, as suggested previously (Ydens et al., 2020).

PNS-MPs in injured nerves have distinct origins

The MacBlue × *Cx3cr1*$^{egfp/+}$ mouse was previously shown to discriminate resident MPs from recently recruited MoD-MPs (Loyher et al., 2018; Rodero et al., 2015) in the lungs, and this observation might also be applicable to distinguish resident PNS-MPs from recently recruited PNS-MPs. Nevertheless, we cannot exclude that the accumulation of EGFP⁺ cells results only from the down-regulation of ECFP expression together with a progressive functional evolution, as supported by transcriptional signature. To address this issue, we performed parabiosis of *Ccr2*$^{-/-}$ host parabiont with the MacBlue × *Cx3cr1*$^{egfp/+}$ donor mouse. Chimerism of circulating Mo's in parabiosis is known to

Downloaded from http://rupress.org/jem/article-pdf/217/11/e20200471/1047202/jem_20200471.pdf by Curie Bib Paris user on 08 December 2020

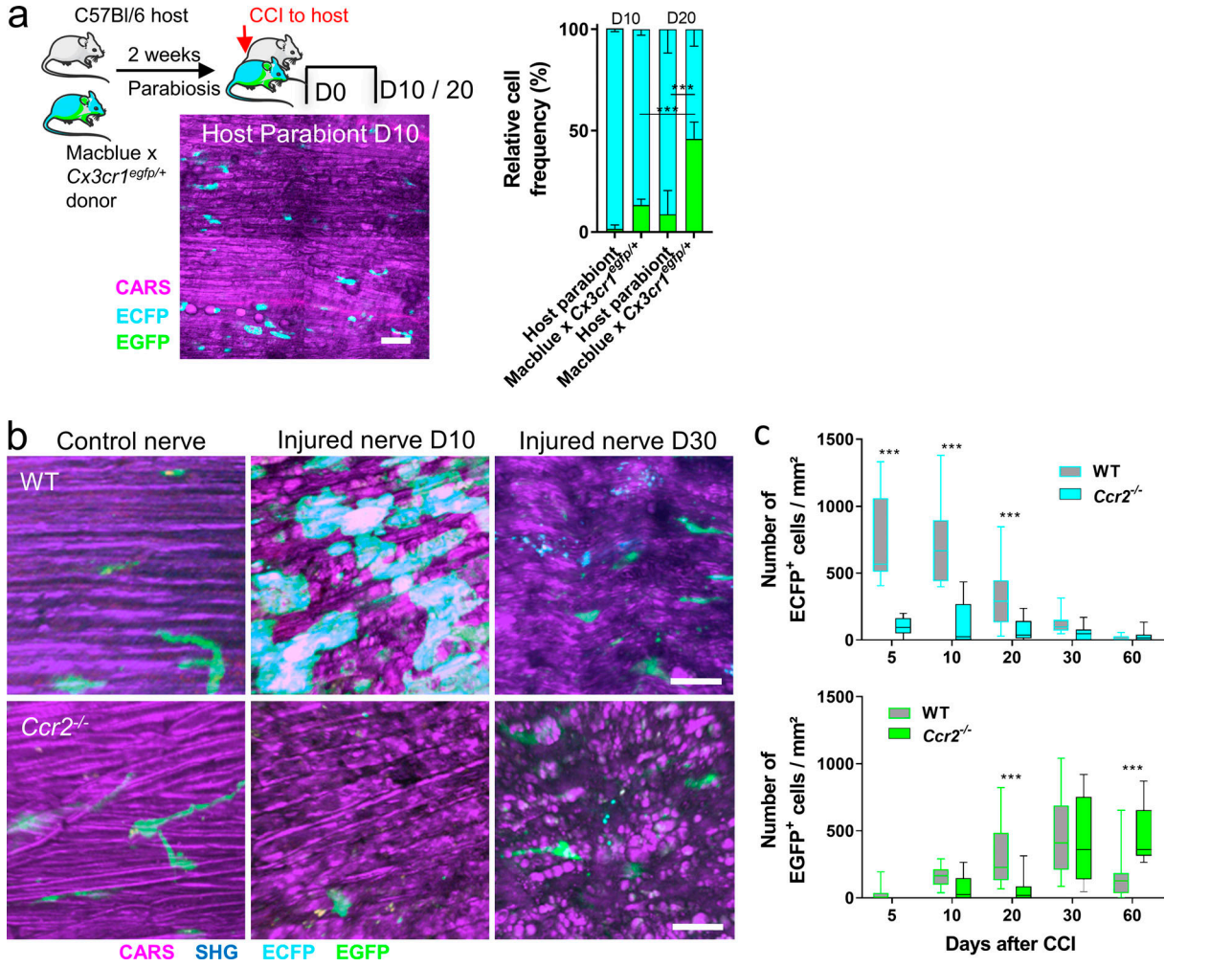


Figure 3. **MPs in the injured nerve have dual origin. (a)** CCI is performed on *Ccr2*$^{-/-}$ host in parabiosis with MacBlue × *Cx3cr1*$^{egfp/+}$ donor mice, and fluorescent cells are tracked 10 and 20 d after nerve injury. Representative TPLSM tiled and stitched image reconstitution (scale bar = 50 µm) and quantification of the relative proportion of EGFP$^+$ and ECFP$^+$ cells in injured sciatic nerve cryosections in host parabiont and nonparabiotic MacBlue × *Cx3cr1*$^{egfp/+}$ mice (data represent a pool from three or four parabioses and four nonparabioses per time point processed independently; ANOVA with Bonferroni's multiple comparison test was performed). **(b)** TPLSM images show the defect in ECFP$^+$ cell accumulation in MacBlue × *Cx3cr1*$^{egfp/+}$ *Ccr2*$^{-/-}$ mouse compared with MacBlue × *Cx3cr1*$^{egfp/+}$. Scale bars = 30 µm. **(c)** Quantification (number/mm^2) of ECFP$^+$ (upper panel) and EGFP$^+$ cells (lower panel) from nerve cryosection (n = 4–5 mice per time point processed independently; P values of two-way ANOVA with Bonferroni multiple comparison tests are indicated). ***, P < 0.001.

be lower than chimerism of circulating lymphocytes. Although 50% chimerism of circulating lymphocytes was reached in our system within 2 wk, the chimerism of Mo's was variable and lower than expected in the CCR2$^{-/-}$ host mice (18 ± 14%), suggesting a reduced life span of fluorescent Mo's from the donor mouse compared with nonfluorescent host Mo's. Quantifying the absolute number of fluorescent cells infiltrating the nerve of the host parabiont was not relevant; hence, we normalized to the relative frequency of ECFP$^+$ and EGFP$^+$ cells in each host parabiont and compared with the relative frequency observed in MacBlue × *Cx3cr1*$^{egfp/+}$ (Fig. 3 a). ECFP$^+$ cells were detected in the host parabiont 10 and 20 d after CCI, while EGFP$^+$ cells were barely detected, resulting in a lower EGFP/ECFP cell ratio compared with the ones observed in MacBlue × *Cx3cr1*$^{egfp/+}$ mice at the same days after injury. This observation strongly supports that EGFP$^+$ cell accumulation does not result from ECFP downregulation alone but is mainly independent of blood circulating cells and might rather represent resident MPs undergoing local proliferation upon injury, as suggested by the higher cell cycle–associated gene cluster in this subset (Fig. 2 f). Contrastingly, to confirm the recent Mo origin of the ECFP$^+$ cells, we performed CCI to MacBlue × *Cx3cr1*$^{egfp/+}$ × *Ccr2*$^{-/-}$. CCR2-deficient mice lack peripheral Mo's (Shi et al., 2011). Accordingly, ECFP$^+$ cell accumulation was almost entirely abrogated in MacBlue × *Cx3cr1*$^{egfp/+}$ × *Ccr2*$^{-/-}$ mice, confirming their recent CCR2-dependent recruitment (Fig. 3 b), while the accumulation of EGFP$^+$ cells was delayed but comparable to CCR2-proficient mice, strengthening that their accumulation is independent of peripheral Mo's (Fig. 3 c). We conclude that the dual-reporter mouse model allows us to monitor endogenous subsets of PNS-associated myeloid cells, including the recently recruited MonoMac waterfall for ECFP$^+$ cells and tissue-resident MPs for EGFP$^+$ cells, according to previous reports (Kolter et al., 2020; Ydens et al., 2020).

Downloaded from http://rupress.org/jem/article-pdf/217/11/e20200471/1047202/jem_20200471.pdf by Curie Bib Paris user on 08 December 2020

Recently recruited MoD-MPs and resident PNS-MPs differentially contribute to WD

We investigated more deeply the function of these different MP subsets by monitoring the impact of CCR2 deficiency on both myelin and neurofilament regeneration. Defects in MoD cell accumulation in CCR2-deficient mice resulted in a significant delay in myelin degeneration and regeneration (Fig. 4, a and b), but no difference was observed regarding the neurofilaments according to NF200 staining (Fig. 4, c and d). To further investigate the role of recently recruited MoD-MPs in myelin degradation, we performed functional live imaging of the nerve during the first week following injury. ECFP$^+$ cell tracking unveiled different motion behaviors. Some small, round ECFP$^+$ cells crawled between myelinated fibers (Fig. S3 a and Video 1) in accordance with a progressive distal migration from the constriction (Fig. 2, c and d). Some ECFP$^+$ cells were still in the region of myelin breakdown, started to encapsulate the fiber (Fig. S3 b and Video 1), and progressively engulfed the myelin sheath by extending long cellular protrusions (Fig. S3 c and Video 1). ECFP$^+$ cells progressively tore apart the myelin sheath, grabbing large lipid vesicles (Video 2), leading to the accumulation of large, foamy MPs full of myelin vesicles (Fig. 4 e). This phagocytic morphology peaked at day 10 in ECFP$^+$ cells and was barely observed in EGFP$^+$ resident MPs at any time point (Fig. 4 e). 3D masking based on the quality of the myelin showed that ECFP$^+$ cells tend to be more present in regions with more degraded myelin (Fig. S3 d). Indeed, myelin roundness correlated with ECFP$^+$ cell density, arguing for their contribution in this process (Fig. S3 e). So far, selective targeting of resident MP without affecting recruited MoD-MPs is not available. To investigate the role of EGFP$^+$ resident MPs in WD, we performed local intramuscular injections of anti-CSF1R at the beginning of the remyelination phase (day 20 after injury), when ECFP$^+$ cells had mostly contracted and EGFP$^+$ resident MPs were in expansion (Fig. 4 f). As previously shown in other models (Loyher et al., 2018), ECFP$^+$ cells were less affected by anti-CSF1R treatment than EGFP$^+$ resident MPs (Fig. 4 g). Myelin regeneration at day 30 was impaired by the late depletion of resident MPs likely due to the requirement of the axon to guide Schwann cell folding (Fig. 4 h), but the deleterious impact on neurofilament regeneration was even more striking (Fig. 4 i). Overall, our data show a distinct contribution of recruited MoD-MPs and resident MPs in the processes of tissue clearance and regeneration, respectively, during WD.

So far, the study of resident PNS-MPs was based on hematopoietic chimera after whole-body irradiation, which leads to the replacement of truly resident MPs by hematogenous MPs. The best asset of this dual-fluorescent model is to allow the discrimination of endogenous MP subsets from distinct origin without adding this potential bias and propose a spatiotemporal characterization of their function. Tracking ECFP$^+$ cells was however limited by the fact that Mo's and MoD-MPs cannot be accurately distinguished and that some neutrophils with low expression of ECFP can be visible. On the other hand, the quantification of EGFP$^+$ cells can be contaminated by CX3CR1$^+$ natural killer cells, although the obvious elongated morphology of these cells is minimal (Laviron et al., 2019). Parabiosis experiments support that the majority of EGFP$^+$ cells arise not from the down-regulation of ECFP in recently recruited MoD-MPs that also express EGFP according to their monocytic origin (Jung et al., 2000) but rather from the local proliferation of resident MP. Whether EGFP$^+$ cells are embryonic derived or originate from long-lasting MPs that are progressively replaced by hematogenous Mo's has recently been solved by Guilliams' group (Ydens et al., 2020) using fate-mapping models that efficiently tagged the PNS-MPs. The absence of ECFP$^+$ cells in steady-state nerve suggests that ECFP down-regulation might occur over time, and it might reflect an adaptation of these cells to their local environment, such as responsiveness to CSF1 (Hawley et al., 2018). The number of resident MPs is not affected in steady-state CCR2-deficient mice, consistent with the very slow replacement rate of this subset (Kolter et al., 2020; Ydens et al., 2020). Ydens et al. further investigated resident MP activation upon nerve crush, which is slightly different from the CCI model in particular regarding the type of injury and the kinetics of regeneration. They observed that endoneurial and epineurial resident MPs differentially responded during the first days following the injury according to single-cell RNA-seq analysis and raised the question of the role of the recently recruited MoD-MPs (Ydens et al., 2020). In the present study, we did not discriminate the two resident subsets in the bulk RNA-seq suggesting that we may miss specific functional signatures. Histological analysis confirmed the large accumulation of endoneurial MPs in close contact with neurofibers, but epineurial MPs also tended to accumulate at the periphery close to the knots. This differences are likely due to the fact that CCI represents a chronic insult occurring by constant friction of the nerve likely involving MP from all tissue layers in contrast to the crush model. Kolter et al. identify in the skin, a CX3CR1^{high} embryonic-derived subset interacting with sensory nerves that self-maintain with a very low turnover rate (Kolter et al., 2019). They showed a key role of this dermal resident MP in axon sprouting after injury (Kolter et al., 2019). Accordingly, the transcriptomic signature of resident MPs in the sciatic nerve suggested a role in ECM regeneration to favor guidance of the axon. This was confirmed by the complete ablation of axon regeneration after depletion of resident MPs with anti-CSF1R. Axon sprouting is necessary to let Schwann cells properly fold around and regenerate the myelin sheath; therefore, myelin sheath regeneration was impacted and was associated with a longer persistence of ECFP$^+$ phagocytic cells compared with control. Beyond phagocytosis of myelin debris, MP regulate Schwann cell dedifferentiation (Klein and Martini, 2016) and maturation for efficient regeneration (Stratton et al., 2018). As MPs were also proposed to collaborate in Schwann cell autophagy (Brosius Lutz et al., 2017; Gomez-Sanchez et al., 2015) during the demyelination phase, it is difficult to determine which of these different attributions is mediated by the different MP subsets. Real-time visualization of recently recruited MoD-MPs stripping the myelin and accumulating lipid-rich vesicles like foam cells provides clues about how ovoid formation and destruction (Tricaud and Park, 2017) of the myelin sheath occurs and suggest that these events are not a result of Schwann cell autophagy alone. WD in CCR2-deficient mice is significantly

Downloaded from http://rupress.org/jem/article-pdf/217/11/e20200471/1047202/jem_20200471.pdf by Curie Bib Paris user on 08 December 2020

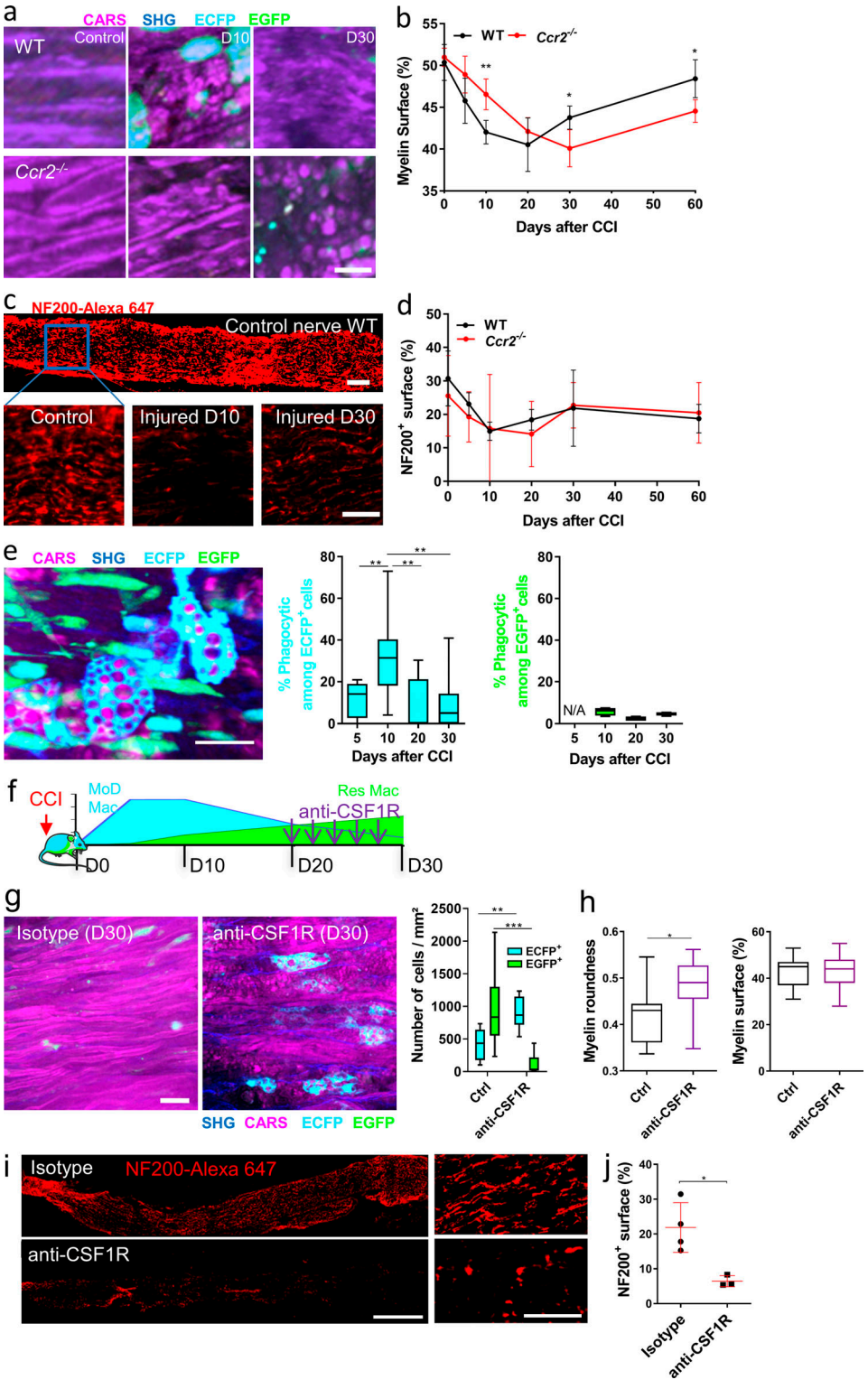


Figure 4. **Recruited and resident MPs exert distinct functions in nerve regeneration. (a)** TPLSM images show the qualitative defect in myelin degeneration in CCR2-deficient compared with CCR2 proficient mice. Images are zoomed in representative region from Fig. 3 b. Scale bar = 15 µm. **(b)** Comparative quantification (mean ± 95% CI) of the myelin surface between WT and *Ccr2*$^{-/-}$ mice based on TPLSM images of nerve cryosections (n = 3–4 mice per time point processed independently; P values of two-way ANOVA with Bonferroni multiple comparison tests between WT and *Ccr2*$^{-/-}$ mice are indicated). **(c)** Fluorescent images of NF200 staining of sciatic nerves in WT mice show the axon degeneration and regeneration after CCI. Scale bars = 100 µm for the upper image and 50 µm for lower images. **(d)** Quantification (mean ± 95% CI) of the NF200 staining between WT and *Ccr2*$^{-/-}$ mice based on fluorescent images of nerve cryosections (n = 3–5 mice per time point, processed independently; two-way ANOVA with Bonferroni multiple comparison tests unveiled no significant difference between WT and *Ccr2*$^{-/-}$ mice). **(e)** TPLSM image (left panel) shows example of foamy/phagocytic ECFP$^+$ cell morphologies compared with EGFP$^+$ cells (scale bar = 20 µm) and (right panel) shows the quantification of the proportion of phagocytic cells among ECFP$^+$ cells (middle panel) and EGFP$^+$ cells (right panel)

Downloaded from http://rupress.org/jem/article-pdf/217/11/e20200471/1047202/jem_20200471.pdf by Curie Bib Paris user on 08 December 2020

following CCI (n = 3–4 mice per time point, processed independently; P values of one-way ANOVA with Bonferroni multiple comparison tests are indicated). **(f)** Schema of anti-CSF1R treatment to prevent resident MPs accumulation 30 d after CCI. **(g)** Representative TPLSM images (scale bar = 20 µm) and quantification of cell numbers show the complete abrogation of EGFP$^+$ MP accumulation in anti-CSF1R treated mice 30 d after CCI (n = 3 mice representative of two independent experiments; P values of two-way ANOVA with Bonferroni's multiple comparison test are indicated). **(h)** Quantification of myelin roundness and surface show qualitatively reduced myelin regeneration after anti-CSF1R treatment (n = 3 mice, representative of two independent experiments; P values of unpaired t tests are indicated). **(i)** Left: Fluorescent images of NF200 staining of sciatic nerve cryosection in WT mice treated or not with anti-CSF1R 30 d after CCI. Scale bars = 500 µm for left images and 100 µm for right images. **(j)** Quantification (mean ± 95% CI) of NF200 staining based on fluorescent images of nerve cryosections (n = 3 mice, representative of two independent experiments; P values of unpaired t test are indicated). See also Fig. S3, Video 1, and Video 2. *, P < 0.05; **, P < 0.01; ***, P < 0.001.

delayed but still occurs suggesting other subsets being involved. It is unlikely that resident PNS-MPs can compensate in that case, as we observed that they accumulate in significant number after the demyelination in CCR2-deficient mice. Neutrophils in this context have been shown to compensate the defect in Mo's, confirming their implication in this process too (Lindborg et al., 2017). Although recruited MoD-MP function seems to be compensated, the deletion of resident MPs completely abrogated neurofiber regeneration, supporting their essential role in WD regeneration. In the crush injury model (Ydens et al., 2020), the transcriptomic signatures of resident MPs have been shown to evolve over time, from the onset of the inflammatory response recruiting MoD-MPs to the neurofiber regeneration process that we uncovered at a later time point.

Whether our observations are transposable to the central nervous system (CNS) needs to be verified. Moreover, the cell partners involved in WD in the CNS and PNS are different (Avellino et al., 1995) and resident MPs appear different from microglia (Ydens et al., 2020). Direct visualization of CX3CR1-EGFP$^+$ cell accumulation in the CNS was associated with axonal dieback after spinal cord injury (Evans et al., 2014), but the accurate discrimination of MoD cells with microglia using the Cx3cr1$^{egfp/+}$ mouse reporter is difficult to assess, as both resident and recruited MoD-MPs may express similar levels of EGFP. Axonal retraction was shown to be dependent on the activity of MMP9 (Busch et al., 2009), a gene enriched in recruited MoD-MPs, arguing that similar molecular mechanisms in recruited MP–mediated neurodegeneration are shared between the PNS and CNS.

Deciphering that MPs of distinct origin carry out different phases of the WD independently reconciles the inflammatory and anti-inflammatory MP paradox (Klein and Martini, 2016) and provides new inputs in targeting myeloid subsets selectively for therapeutic applications in a wide range of neurodegenerative disorders.

Materials and methods

Mice

Female C57Bl6 mice were purchased from Janvier Labs. Csf1r-Gal4VP16/UAS-ECFP double-transgenic mice named MacBlue (Ovchinnikov et al., 2008), *Cx3cr1^{egfp}* (Jung et al., 2000), and *Ccr2$^{-/-}$* mice were intercrossed to generate MacBlue × *Cx3cr1$^{egfp/+}$*, MacBlue × *Cx3cr1$^{egfp/+}$* × *Ccr2$^{-/-}$* mouse strains (Loyher et al., 2018), hence are littermates and were bred at Pitié-Salpêtrière animal facility. All mice were maintained under specific pathogen–free conditions, and either male or females were used between 8 and 14 wk old.

CCI

CCI was performed on mice by adapting the Bennet and Xie method (Bennett and Xie, 1988). As described previously (Van Steenwinckel et al., 2015), mice were anesthetized, and their left sciatic nerve (ipsilateral) was exposed under a dissection microscope. Three chromic catgut (6/0, 1.0 metric; CpMedical) ligations were tied loosely at a spacing of 1 mm, proximal to the sciatic trifurcation. The incision was closed with silk sutures. The right sciatic nerve was used as a control (contralateral), and no difference was observed compared with nerves from non-injured mice. The anti-CSF1R antibody (AFS98; BioXcell) or rat IgG2aκ isotype controls were administrated through local injection in the biceps femoris of 25 µl of a PBS solution at 5 mg/kg every 2 d from day 20 to day 30 after CCI.

Ethical statement

All experiment protocols were approved by the French animal experimentation and ethics committee and validated by "Service Protection et Santé Animales, Environnement" with the number APAFJS#1046-2015070316122486 v3 for CCI and A-75-1315 for parabiosis experiments. Sample sizes were chosen to assure reproducibility of the experiments and according to the 3Rs of animal ethics regulation.

Parabiosis

Ccr2$^{-/-}$ female host parabionts were generated with donor MacBlue × *Cx3cr1$^{egfp/+}$* females. 2 wk after parabiosis 50% chimerism was reached according to circulating lymphocytes but fluorescent Ly6C^{high} Mo chimerism was only 18 ± 14%. CCI was performed on host animal and donor fluorescent cell infiltration was monitored in injured nerve by imaging. No donor fluorescent cells were detected in contralateral nerves.

Flow cytometry

Sciatic nerves were harvested and digested in PBS (GIBCO BRL Invitrogen) with 1 mg/ml collagenase IV (Sigma–Aldrich) for 1 h at 37°C and filtered through a 70-µm-pore cell strainer (Becton Dickinson). The total cell suspension was incubated with 1 µg/ml purified anti-CD16/32 (2.4G2; BD Biosciences) for 10 min at 4°C, and then surface staining was performed by an additional 20-min incubation with appropriate dilution of the surface marker antibodies. Cells were then washed once in FACS buffer and analyzed directly by flow cytometry. The panel of antibodies used was anti-CD11b (clone M1/70), anti-Ly6C (clone AL-21), anti-Ly6G (clone 1A8), anti-IA[b] (clone AF6-120.1), anti-CD45 (clone 30-F11), anti-CD64 (clone X54-5/7.1), anti-Siglec-F (clone E50-2440), anti-CD36 (clone CRF D-2712; PharMingen, BD

Downloaded from http://rupress.org/jem/article-pdf/217/11/e20200471/1047202/jem_20200471.pdf by Curie Bib Paris user on 08 December 2020

Bioscience), and anti-CD206 (clone C068C2; Biolegend). Calculation of absolute cell number was performed by adding to each vial a fixed number (10,000) of nonfluorescent 10-µm polybead carboxylate microspheres (Polysciences) according to the following formula: number of cells = (number of acquired cells × 10,000)/(number of acquired beads). Number of cells obtained for each sample was normalized per milligram of tissue. Flow cytometry acquisition was performed on the flow cytometer FACS LSRFortessa X-20 (BD Bioscience) with DIVA Flow Cytometry software. Flow cytometry data were analyzed with FlowJo software (Tree Star).

Nerve cryosections and immunostaining

Sciatic nerves from the different fluorescent mouse strains were harvested and fixed in 4% paraformaldehyde for 24 h at 4°C, then dehydrated in 30% sucrose solution (1× PBS; pH 7.4) overnight at 4°C, before being immerged in optimal cutting temperature compound (Tissue-Tek O.C.T. Compound; Sakura Finetek) and frozen. Longitudinal sciatic nerves cryosections 8 µm thick were made using a Leica cryostat CM 3050S, washed, mounted with Fluoromount with DAPI (Sigma–Aldrich), and directly imaged. For neurofilament-200 (NF200) staining, cryosections were incubated for 2 h at room temperature in blocking buffer (NDS 3% and 0.1% Triton X-100 in 1× PBS) and then incubated overnight at 4°C in incubation buffer (NDS 3% and 0.1% Triton X-100 in 1× PBS) with polyclonal rabbit anti-NF200 (1/500; Sigma–Aldrich). Cryosections were washed in 1× PBS and incubated with a donkey anti-rabbit Alexa Fluor 647 secondary antibody (1/500; Thermo Fisher Scientific).

Multiphoton and epifluorescence imaging

For live imaging, nerves were carefully collected and immobilized in an imaging chamber perfused with oxygenated (95% O_2 plus 5% CO_2) RPMI medium containing 10% FCS. Local temperature was monitored and maintained at 37°C. The two-photon laser scanning microscopy (TPLSM) set-up used was a Zeiss 7MP (Carl Zeiss) coupled to a Ti/sapphire crystal multiphoton laser (Coherent ChameleonU), which provides 140-fs pulses of NIR light, selectively tunable between 680 and 1,050 nm and an optical parametric oscillator (OPO-MPX; Coherent) selectively tunable between 1,050 and 1,600 nm. The nonlinear optical and OPO beams were spatially aligned and temporally synchronized using a delay line (Coherent), allowing for a CARS imaging approach. The nonlinear optical beam was set at 870 nm and the OPO beam at 1,167 nm to detect the vibrational signature of lipid-rich structures at a frequency of 2,925 cm^{-1} with an emission wavelength at 693 nm. The specificity of the CARS signal is controlled by desynchronizing the two beams (see Fig. S1 a). The system included a set of external nondescanned detectors in reflection with a combination of a long-path (LP)–600-nm followed by LP-462-nm and LP-500-nm dichroic mirrors to split the light and collect the SHG signal with a 417/60-nm emission filter, ECFP with a 480/40-nm emission filter, EGFP with a 525/50-nm emission filter, and the CARS signal with an LP-645-nm emission filter. Real-time movies were performed by imaging every 30 s by five consecutive 3-µm z-spacing stacks (total 12 µm thickness). 3D images of intact nerves were generated by 1-µm z-spacing stacks (up to 10 µm thickness). Epifluorescent images were taken on cryosections using a Zeiss Axio Z1 fluorescent microscope (Carl Zeiss) and Zen software. Fluorescent signals were acquired using an excitation band-path (ExBP) 475/40, emission band-path (EmBP) 530/50 for EGFP, an ExBP 436/25, EmBP 480/40 for ECFP, and an ExBP 640/30, EmBP 690/50 for NF200 AF647 light cube filters. Acquisition settings were set on unstained cryosections.

Image quantification

Tiled images were generated by tiles scanning of the area and automatically stitched during acquisition by Zen Black software (Carl Zeiss). For myelin, NF200, and fluorescent MP quantifications, images were taken either on 5-µm-thick cryosections or 3D sections of intact nerves. "Quantitative" myelin and NF200 coverage (as defined by percentage of myelin surface and percentage of NF200 surface, on cryosection) and "qualitative" myelin calculations (as defined by roundness on 3D images) were performed with ImageJ software using the automatic default threshold for surface calculation and roundness formula. Briefly, surface is the proportion of the field covered by the fluorescent signal, and roundness is the shape of the myelin structure (healthy myelin sheaths display a low roundness score, and myelin vesicles display a high roundness score). Myelin surface was calculated as a mean of 10 different fields randomly chosen (representing up to 20% of the nerve section) across three different sections for each nerve. NF200 surface was calculated as a mean of 10–15 consecutive fields along the whole nerve section (representing >50% of the total section). Roundness are calculated across three different fields in the vicinity of the three constriction nodes for each nerve. Surface masking of myelin sheets was performed on a 3D image using Imaris software (Bitplane). $EGFP^+$ and $ECFP^+$ cells were manually counted using ImageJ software, in three or four different fields of nerve cryosections in the vicinity of the three constriction nodes for each nerve and normalized to the surface of tissue. Phagocytic cells were manually counted based on vesicular morphology. $EGFP^+$ and $ECFP^+$ cell distance from constriction was automatically computed using distance transformation plug-in from Imaris software. For all quantifications, data represent mean from at least three different mice for each time point from independent preparations.

RNA-seq sample preparation and analysis

$ECFP^+$ and $EGFP^+$ MPs were sorted using FACS ARIA (BD Biosciences) according to the gating strategy (Fig. 1 e). Three independent sortings were prepared. For each, cell suspension of three sciatic nerves from MacBlue × *Cx3cr1*$^{egfp/+}$ mice 14 d after CCI were pooled. Sorted cells were lysed in 100 µl of RA1/TCEP buffer (NucleoSpin RNA XS; Macherey-Nagel), snap frozen in liquid nitrogen, and stored at −80°C until RNA extraction. All samples were processed in parallel and RNA extraction (without carrier RNA but with on-column DNase treatment) was performed according to the manufacturer's instructions (NucleoSpin RNA XS, Macherey-Nagel). Input cell numbers were adjusted to be the same for all samples (~400 cells). RNA was eluted in RNase-free water. Preparation of cDNA libraries for

Downloaded from http://rupress.org/jem/article-pdf/217/11/e20200471/1047202/jem_20200471.pdf by Curie Bib Paris user on 08 December 2020

RNA-seq was done using the SmartSeq method according to the manufacturer's instructions (SMART-Seq v4 Ultra Low Input RNA Kit for Sequencing; Clontech/TaKaRa). Due to the low number of cells, the total amount of eluted RNA was used as starting material for reverse transcription, followed by 18 cycles of preamplification. 1 ng cDNA was used for RNA-seq library preparation, according to the manufacturer's instructions (Nextera XT DNA Library Preparation; Illumina). Final library preparations were sequenced on a Nextseq 500 Illumina with MidOutPut cartridge (2 × 130 million of 75 base reads) with two runs (4plex and 5plex), corresponding to 2 × 30 million (paired-end) reads per sample after demultiplexing. For analysis, the quality of raw data has been evaluated with FastQC. Poor-quality sequences have been trimmed or removed with Trimmomatic software to retain only good-quality paired reads. Star v2.5.3a has been used to align reads on mm10 reference genome using standard options. Quantification of gene and isoform abundances has been done with rsem 1.2.28, before normalization on library size with DESEq2 Bioconductor package. Finally, differential analysis has been conducted with edgeR Bioconductor package. Multiple hypothesis adjusted P values were calculated with the Benjamini–Hochberg procedure to control false discovery rate (FDR). Heat maps and hierarchical clusters were generated with Multi Experiment Viewer MeV 4.9.0. R software were used for generation of volcano plots. IPA was used to perform functional enrichment analyses; it provided the canonical pathways, molecular/cellular functions, and networks that were statistically overrepresented in the gene signatures. The GEO accession number for the RNA-seq data is GSE152206.

Statistical analysis

All statistical analyses were performed with GraphPad Prism. Multigroup ANOVA was performed using one- or two-way ANOVA followed by Bonferroni multiple comparison tests. For simple comparison analysis, an unpaired *t* test was performed. All experiments were repeated at least twice. For all figures, repeated experiments were pooled to include reproducibility in the variance. For image quantification, all mice were processed independently. The total number of mice is indicated in each figure. *, P < 0.05; **, P < 0.01; ***, P < 0.001; ****, P < 0.0001.

Online supplemental material

Fig. S1 shows CARS signaling specificity and the flow cytometry gating strategy of nerve-infiltrating myeloid cells over time. Fig. S2 shows the relative distribution and the phenotype of MP subsets within the sciatic nerve and additional characteristics of the transcriptomic analysis. Fig. S3 exhibits representative morphological features and dynamic behaviors of recently recruited MPs by two-photon microscopy and CARS imaging. Table S1 lists the 124 differentially expressed genes. Video 1 shows Mo/MP behavior during WD of the sciatic nerve. Video 2 shows an MP stripping the myelin sheath.

Acknowledgments

The authors wish to thank Dr. M. Krummel for helpful discussion and editing of the manuscript and Biological Imaging Development Center staff members (University of California, San Francisco) for advice regarding image quantification. The authors thank the animal facility "NAC" for mice breeding.

This work was supported by grants from Fondation pour la Recherche Médicale "Equipe labelisée" and the Agence Nationale de la Recherche (projects J12R135 CHEMOK PAIN 2 and CE15-0019-02 CMOS). This work benefited from equipment and services from the Centre d'Experimentation Fonctionnelle Pitié-Salpêtrière (animal facility and multiphoton imaging) and the iGenSeq (RNA-seq) and iCONICS (RNA-seq analysis) core facilities at the Institut du Cerveau et de la Moelle épinière, Hôpital Pitié-Salpêtrière (Paris, France), which received funding from the Agence Nationale de la Recherche program "Investissements d'avenir" ANR-10-IAIHU-06.

Author contributions: A. Boissonnas supervised the study, designed and performed experiments, analyzed and interpreted the data, and wrote the manuscript. F. Louboutin performed experiments, analyzed and interpreted data, and edited the manuscript. M. Laviron, E. Reboussin, P.L. Loyher, A. Réaux-Le Goazigo, and S. Barthelemy performed experiments. C.S. Lobsiger and B. Combadière contributed to RNA-seq experiment analysis and interpretation. S. Mélik Parsadaniantz and C. Combadière provided reagents, designed research, analyzed and interpreted the data, supervised the study, and edited the manuscript.

Disclosures: The authors declare no competing interests exist.

Submitted: 11 March 2020
Revised: 29 May 2020
Accepted: 17 June 2020

References

Avellino, A.M., D. Hart, A.T. Dailey, M. MacKinnon, D. Ellegala, and M. Kliot. 1995. Differential macrophage responses in the peripheral and central nervous system during wallerian degeneration of axons. *Exp. Neurol.* 136:183–198. https://doi.org/10.1006/exnr.1995.1095

Bain, C.C., A. Bravo-Blas, C.L. Scott, E.G. Perdiguero, F. Geissmann, S. Henri, B. Malissen, L.C. Osborne, D. Artis, and A.M. Mowat. 2014. Constant replenishment from circulating monocytes maintains the macrophage pool in the intestine of adult mice. *Nat. Immunol.* 15:929–937. https://doi.org/10.1038/ni.2967

Bélanger, E., F.P. Henry, R. Vallée, M.A. Randolph, I.E. Kochevar, J.M. Winograd, C.P. Lin, and D. Côté. 2011. In vivo evaluation of demyelination and remyelination in a nerve crush injury model. *Biomed. Opt. Express.* 2:2698–2708. https://doi.org/10.1364/BOE.2.002698

Bennett, G.J., and Y.K. Xie. 1988. A peripheral mononeuropathy in rat that produces disorders of pain sensation like those seen in man. *Pain.* 33:87–107. https://doi.org/10.1016/0304-3959(88)90209-6

Brosius Lutz, A., W.S. Chung, S.A. Sloan, G.A. Carson, L. Zhou, E. Lovelett, S. Posada, J.B. Zuchero, and B.A. Barres. 2017. Schwann cells use TAM receptor-mediated phagocytosis in addition to autophagy to clear myelin in a mouse model of nerve injury. *Proc. Natl. Acad. Sci. USA.* 114:E8072–E8080. https://doi.org/10.1073/pnas.1710566114

Busch, S.A., K.P. Horn, D.J. Silver, and J. Silver. 2009. Overcoming macrophage-mediated axonal dieback following CNS injury. *J. Neurosci.* 29:9967–9976. https://doi.org/10.1523/JNEUROSCI.1151-09.2009

Chakarov, S., H.Y. Lim, L. Tan, S.Y. Lim, P. See, J. Lum, X.M. Zhang, S. Foo, S. Nakamizo, K. Duan, et al. 2019. Two distinct interstitial macrophage populations coexist across tissues in specific subtissular niches. *Science.* 363. eaau0964. https://doi.org/10.1126/science.aau0964

Chen, P., X. Piao, and P. Bonaldo. 2015. Role of macrophages in Wallerian degeneration and axonal regeneration after peripheral nerve injury.

Downloaded from http://rupress.org/jem/article-pdf/217/11/e20200471/1047202/jem_20200471.pdf by Curie Bib Paris user on 08 December 2020

Acta Neuropathol. 130:605–618. https://doi.org/10.1007/s00401-015-1482-4

Coleman, M.P., and M.R. Freeman. 2010. Wallerian degeneration, wld(s), and nmnat. *Annu. Rev. Neurosci*. 33:245–267. https://doi.org/10.1146/annurev-neuro-060909-153248

DeFrancesco-Lisowitz, A., J.A. Lindborg, J.P. Niemi, and R.E. Zigmond. 2015. The neuroimmunology of degeneration and regeneration in the peripheral nervous system. *Neuroscience*. 302:174–203. https://doi.org/10.1016/j.neuroscience.2014.09.027

Epelman, S., K.J. Lavine, A.E. Beaudin, D.K. Sojka, J.A. Carrero, B. Calderon, T. Brija, E.L. Gautier, S. Ivanov, A.T. Satpathy, et al. 2014. Embryonic and adult-derived resident cardiac macrophages are maintained through distinct mechanisms at steady state and during inflammation. *Immunity*. 40:91–104. https://doi.org/10.1016/j.immuni.2013.11.019

Evans, T.A., D.S. Barkauskas, J.T. Myers, E.G. Hare, J.Q. You, R.M. Ransohoff, A.Y. Huang, and J. Silver. 2014. High-resolution intravital imaging reveals that blood-derived macrophages but not resident microglia facilitate secondary axonal dieback in traumatic spinal cord injury. *Exp. Neurol*. 254:109–120. https://doi.org/10.1016/j.expneurol.2014.01.013

Gibbings, S.L., S.M. Thomas, S.M. Atif, A.L. McCubbrey, A.N. Desch, T. Danhorn, S.M. Leach, D.L. Bratton, P.M. Henson, W.J. Janssen, et al. 2017. Three Unique Interstitial Macrophages in the Murine Lung at Steady State. *Am. J. Respir. Cell Mol. Biol*. 57:66–76. https://doi.org/10.1165/rcmb.2016-0361OC

Ginhoux, F., and S. Jung. 2014. Monocytes and macrophages: developmental pathways and tissue homeostasis. *Nat. Rev. Immunol*. 14:392–404. https://doi.org/10.1038/nri3671

Gomez Perdiguero, E., K. Klapproth, C. Schulz, K. Busch, E. Azzoni, L. Crozet, H. Garner, C. Trouillet, M.F. de Bruijn, F. Geissmann, et al. 2015. Tissue-resident macrophages originate from yolk-sac-derived erythro-myeloid progenitors. *Nature*. 518:547–551. https://doi.org/10.1038/nature13989

Gomez-Sanchez, J.A., L. Carty, M. Iruarrizaga-Lejarreta, M. Palomo-Irigoyen, M. Varela-Rey, M. Griffith, J. Hantke, N. Macias-Camara, M. Azkargorta, I. Aurrekoetxea, et al. 2015. Schwann cell autophagy, myelinophagy, initiates myelin clearance from injured nerves. *J. Cell Biol*. 210:153–168. https://doi.org/10.1083/jcb.201503019

Hawley, C.A., R. Rojo, A. Raper, K.A. Sauter, Z.M. Lisowski, K. Grabert, C.C. Bain, G.M. Davis, P.A. Louwe, M.C. Ostrowski, et al. 2018. *Csf1r*-mApple Transgene Expression and Ligand Binding In Vivo Reveal Dynamics of CSF1R Expression within the Mononuclear Phagocyte System. *J. Immunol*. 200:2209–2223. https://doi.org/10.4049/jimmunol.1701488

Jung, S., J. Aliberti, P. Graemmel, M.J. Sunshine, G.W. Kreutzberg, A. Sher, and D.R. Littman. 2000. Analysis of fractalkine receptor CX(3)CR1 function by targeted deletion and green fluorescent protein reporter gene insertion. *Mol. Cell. Biol*. 20:4106–4114. https://doi.org/10.1128/MCB.20.11.4106-4114.2000

Klein, D., and R. Martini. 2016. Myelin and macrophages in the PNS: An intimate relationship in trauma and disease. *Brain Res*. 1641(Pt A):130–138. https://doi.org/10.1016/j.brainres.2015.11.033

Kolter, J., R. Feuerstein, P. Zeis, N. Hagemeyer, N. Paterson, P. d'Errico, S. Baasch, L. Amann, T. Masuda, A. Lösslein, et al. 2019. A Subset of Skin Macrophages Contributes to the Surveillance and Regeneration of Local Nerves. *Immunity*. 50:1482–1497.e7. https://doi.org/10.1016/j.immuni.2019.05.009

Kolter, J., K. Kierdorf, and P. Henneke. 2020. Origin and Differentiation of Nerve-Associated Macrophages. *J. Immunol*. 204:271–279. https://doi.org/10.4049/jimmunol.1901077

Laviron, M., C. Combadière, and A. Boissonnas. 2019. Tracking Monocytes and Macrophages in Tumors With Live Imaging. *Front. Immunol*. 10:1201. https://doi.org/10.3389/fimmu.2019.01201

Le, T.T., S. Yue, and J.X. Cheng. 2010. Shedding new light on lipid biology with coherent anti-Stokes Raman scattering microscopy. *J. Lipid Res*. 51:3091–3102. https://doi.org/10.1194/jlr.R008730

Lee, M., and A. Serrels. 2016. Multiphoton Microscopy for Visualizing Lipids in Tissue. *Methods Mol. Biol*. 1467:105–118. https://doi.org/10.1007/978-1-4939-4023-3_9

Lindborg, J.A., M. Mack, and R.E. Zigmond. 2017. Neutrophils Are Critical for Myelin Removal in a Peripheral Nerve Injury Model of Wallerian Degeneration. *J. Neurosci*. 37:10258–10277. https://doi.org/10.1523/JNEUROSCI.2085-17.2017

Loyher, P.L., P. Hamon, M. Laviron, A. Meghraoui-Kheddar, E. Goncalves, Z. Deng, S. Torstensson, N. Bercovici, C. Baudesson de Chanville, B. Combadière, et al. 2018. Macrophages of distinct origins contribute to tumor development in the lung. *J. Exp. Med*. 215:2536–2553. https://doi.org/10.1084/jem.20180534

Martini, R., S. Fischer, R. López-Vales, and S. David. 2008. Interactions between Schwann cells and macrophages in injury and inherited demyelinating disease. *Glia*. 56:1566–1577. https://doi.org/10.1002/glia.20766

Molawi, K., Y. Wolf, P.K. Kandalla, J. Favret, N. Hagemeyer, K. Frenzel, A.R. Pinto, K. Klapproth, S. Henri, B. Malissen, et al. 2014. Progressive replacement of embryo-derived cardiac macrophages with age. *J. Exp. Med*. 211:2151–2158. https://doi.org/10.1084/jem.20140639

Mueller, M., C. Leonhard, K. Wacker, E.B. Ringelstein, M. Okabe, W.F. Hickey, and R. Kiefer. 2003. Macrophage response to peripheral nerve injury: the quantitative contribution of resident and hematogenous macrophages. *Lab. Invest*. 83:175–185. https://doi.org/10.1097/01.LAB.0000056993.28149.BF

Müller, M., C. Leonhard, M. Krauthausen, K. Wacker, and R. Kiefer. 2010. On the longevity of resident endoneurial macrophages in the peripheral nervous system: a study of physiological macrophage turnover in bone marrow chimeric mice. *J. Peripher. Nerv. Syst*. 15:357–365. https://doi.org/10.1111/j.1529-8027.2010.00295.x

Ovchinnikov, D.A., W.J. van Zuylen, C.E. DeBats, K.A. Alexander, S. Kellie, and D.A. Hume. 2008. Expression of Gal4-dependent transgenes in cells of the mononuclear phagocyte system labeled with enhanced cyan fluorescent protein using Csf1r-Gal4VP16/UAS-ECFP double-transgenic mice. *J. Leukoc. Biol*. 83:430–433. https://doi.org/10.1189/jlb.0807585

Rodero, M.P., L. Poupel, P.L. Loyher, P. Hamon, F. Licata, C. Pessel, D.A. Hume, C. Combadière, and A. Boissonnas. 2015. Immune surveillance of the lung by migrating tissue monocytes. *eLife*. 4. e07847. https://doi.org/10.7554/eLife.07847

Sauter, K.A., C. Pridans, A. Sehgal, C.C. Bain, C. Scott, L. Moffat, R. Rojo, B.M. Stutchfield, C.L. Davies, D.S. Donaldson, et al. 2014. The MacBlue binary transgene (csf1r-gal4VP16/UAS-ECFP) provides a novel marker for visualisation of subsets of monocytes, macrophages and dendritic cells and responsiveness to CSF1 administration. *PLoS One*. 9. e105429. https://doi.org/10.1371/journal.pone.0105429

Shi, C., T. Jia, S. Mendez-Ferrer, T.M. Hohl, N.V. Serbina, L. Lipuma, I. Leiner, M.O. Li, P.S. Frenette, and E.G. Pamer. 2011. Bone marrow mesenchymal stem and progenitor cells induce monocyte emigration in response to circulating toll-like receptor ligands. *Immunity*. 34:590–601. https://doi.org/10.1016/j.immuni.2011.02.016

Stassart, R.M., R. Fledrich, V. Velanac, B.G. Brinkmann, M.H. Schwab, D. Meijer, M.W. Sereda, and K.A. Nave. 2013. A role for Schwann cell-derived neuregulin-1 in remyelination. *Nat. Neurosci*. 16:48–54. https://doi.org/10.1038/nn.3281

Stratton, J.A., A. Holmes, N.L. Rosin, S. Sinha, M. Vohra, N.E. Burma, T. Trang, R. Midha, and J. Biernaskie. 2018. Macrophages Regulate Schwann Cell Maturation after Nerve Injury. *Cell Rep*. 24:2561–2572.e6. https://doi.org/10.1016/j.celrep.2018.08.004

Tricaud, N., and H.T. Park. 2017. Wallerian demyelination: chronicle of a cellular cataclysm. *Cell. Mol. Life Sci*. 74:4049–4057. https://doi.org/10.1007/s00018-017-2565-2

Van Steenwinckel, J., C. Auvynet, A. Sapienza, A. Reaux-Le Goazigo, C. Combadière, and S. Melik Parsadaniantz. 2015. Stromal cell-derived CCL2 drives neuropathic pain states through myeloid cell infiltration in injured nerve. *Brain Behav. Immun*. 45:198–210. https://doi.org/10.1016/j.bbi.2014.10.016

Vass, K., W.F. Hickey, R.E. Schmidt, and H. Lassmann. 1993. Bone marrow-derived elements in the peripheral nervous system. An immunohistochemical and ultrastructural investigation in chimeric rats. *Lab. Invest*. 69:275–282.

Ydens, E., L. Amann, B. Asselbergh, C.L. Scott, L. Martens, D. Sichien, O. Mossad, T. Blank, S. De Prijck, D. Low, et al. 2020. Profiling peripheral nerve macrophages reveals two macrophage subsets with distinct localization, transcriptome and response to injury. *Nat. Neurosci*. 23:676–689. https://doi.org/10.1038/s41593-020-0618-6

Downloaded from http://rupress.org/jem/article-pdf/217/11/e20200471/1047202/jem_20200471.pdf by Curie Bib Paris user on 08 December 2020

JEM

Supplemental material

Downloaded from http://rupress.org/jem/article-pdf/217/11/e20200471/1047202/jem_20200471.pdf by Curie Bib Paris user on 08 December 2020

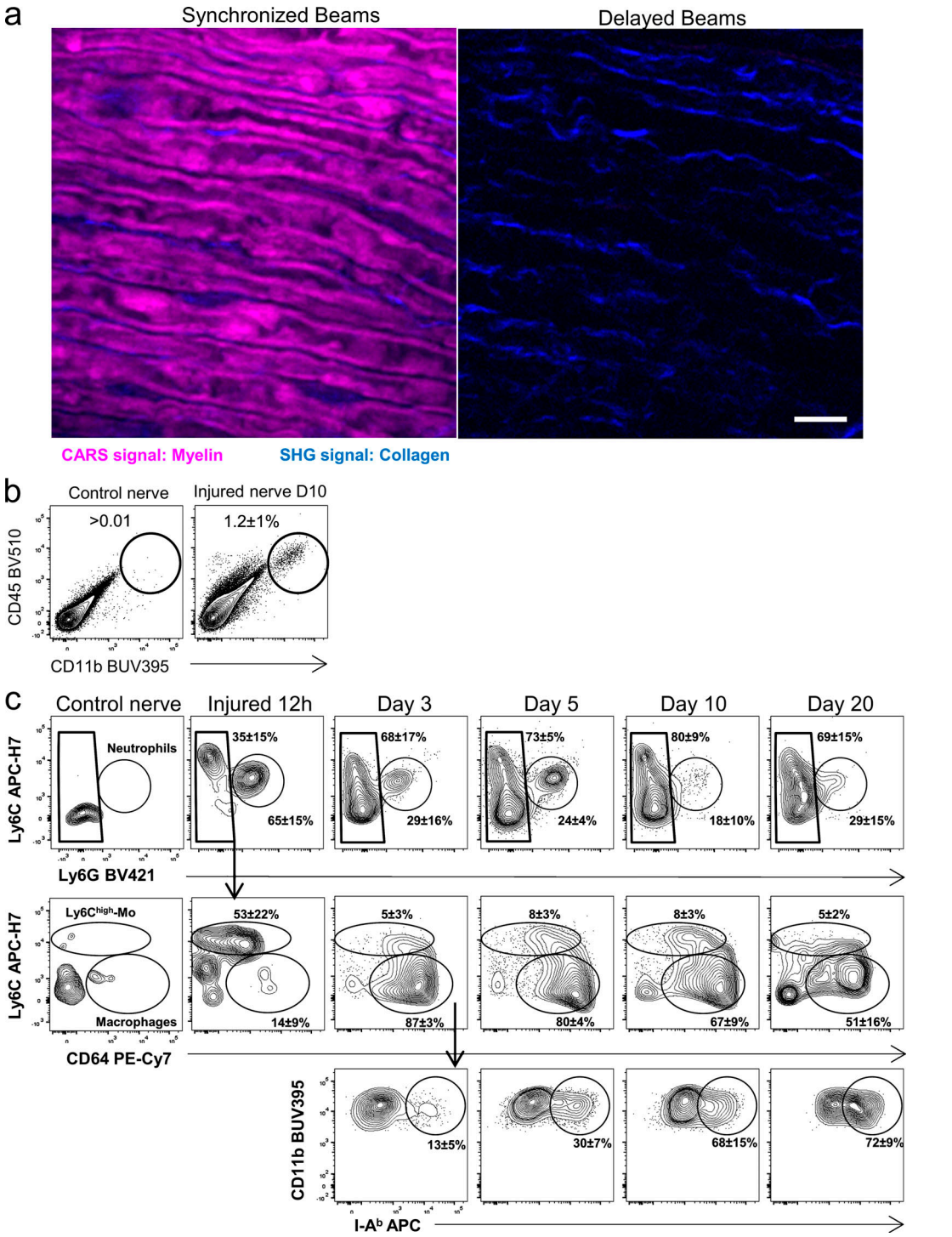


Figure S1. **MP accumulation during WD**. **(a)** TPLSM images show the specificity of CARS signal from the myelin sheath and the SHG from collagen fibers in the sciatic nerve of a C57Bl6 mouse. Scale bar = 10 µm. **(b)** Accumulation of $CD45^+$ $CD11b^+$ cells monitored by flow cytometry in injured nerves, compared with contralateral healthy nerves 10 d after CCI (n = 6 mice out of two experiments; mean percentage ± SD are indicated). **(c)** kinetic of myeloid cell infiltration following CCI monitored by flow cytometry. Dot plots are gated on $CD45^+$ $CD11b^+$ cells. Neutrophils are excluded by Ly6G expression, inflammatory Mo's are defined as $Ly6C^{high}$ $CD64^{low}$, and MPs are defined as $Ly6C^{low/-}$ $CD64^+$. $I\text{-}A^b$ acquisition on MPs is followed. Plots with a too-low number of cells are not depicted (n = 6 mice out of two experiments; mean percentage ± SD are indicated).

Downloaded from http://rupress.org/jem/article-pdf/217/11/e20200471/1047202/jem_20200471.pdf by Curie Bib Paris user on 08 December 2020

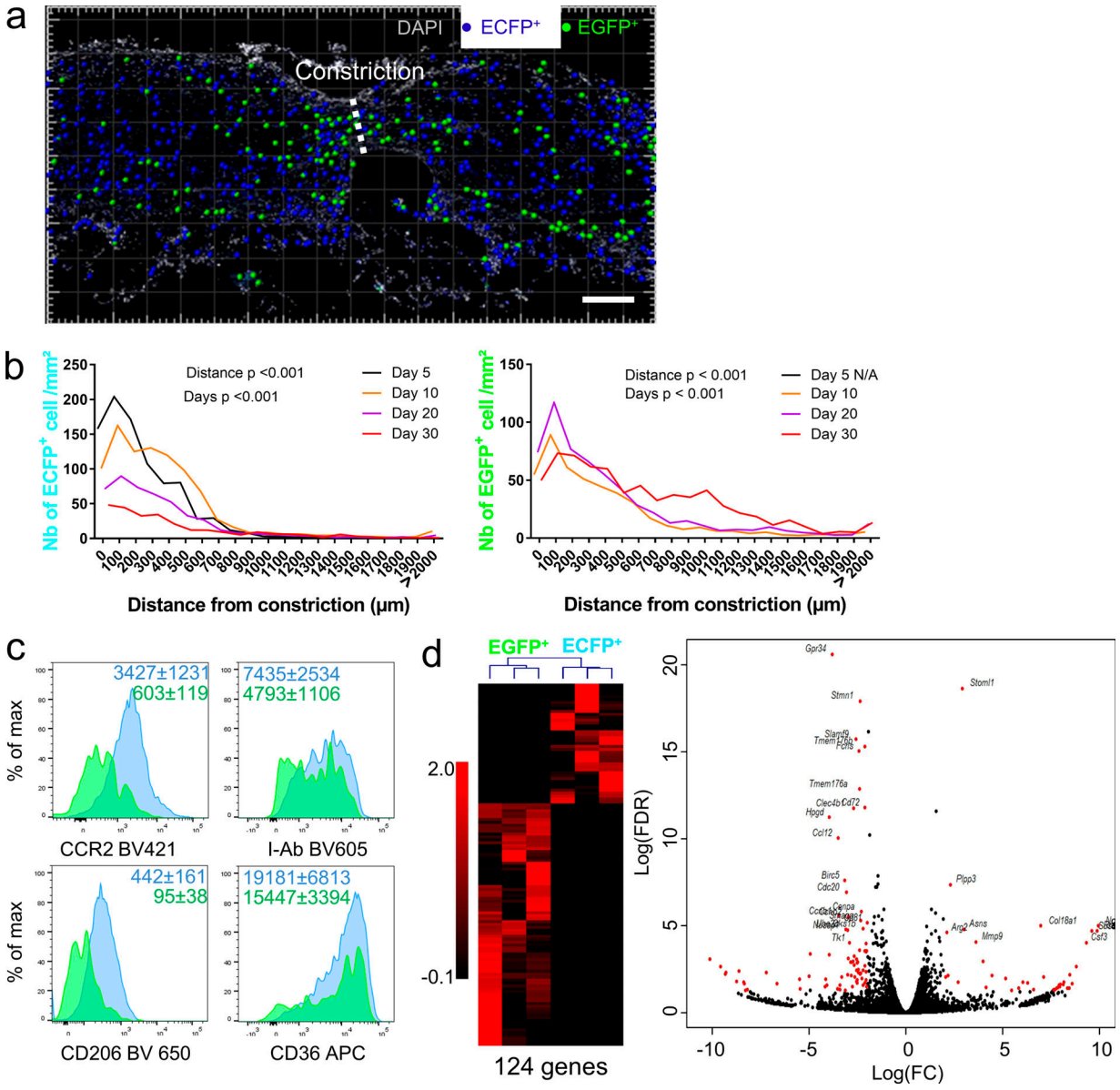


Figure S2. **MP subsets are functionally distinct. (a)** Images of sciatic nerve cryosection 20 d after CCI of MacBlue x *Cx3cr1*$^{egfp/+}$ mice shows the distribution of ECFP$^+$ (blue spots) and EGFP$^+$ (green spots) relative to the constriction site (white dashed line). Scale bar = 150 µm. **(b)** Graphs show the relative frequency of ECFP$^+$ (left panel) and EGFP$^+$ (right panel) cells as a function of the distance from to the constriction at indicated days after injury (n = 3–5 mice per time point processed independently; P values of two-way ANOVA are indicated). **(c)** Phenotypic characterization gated on of EGFP$^+$ and ECFP$^+$ MPs (Fig. 1 e) in sciatic nerves 10 d after CCI. Mean fluorescence intensity ± SD are indicated for each subset (n = 6 mice out of two experiments). **(d)** Hierarchical clustering and Volcano plot of the 124 genes differentially expressed between ECFP$^+$ and EGFP$^+$ sorted MPs at d14 after CCI (n = 3 independent sorting from a pool of three mice each; fold change [FC] threshold is set to 2, and FDR P value < 0.05).

Downloaded from http://rupress.org/jem/article-pdf/217/11/e20200471/1047202/jem_20200471.pdf by Curie Bib Paris user on 08 December 2020

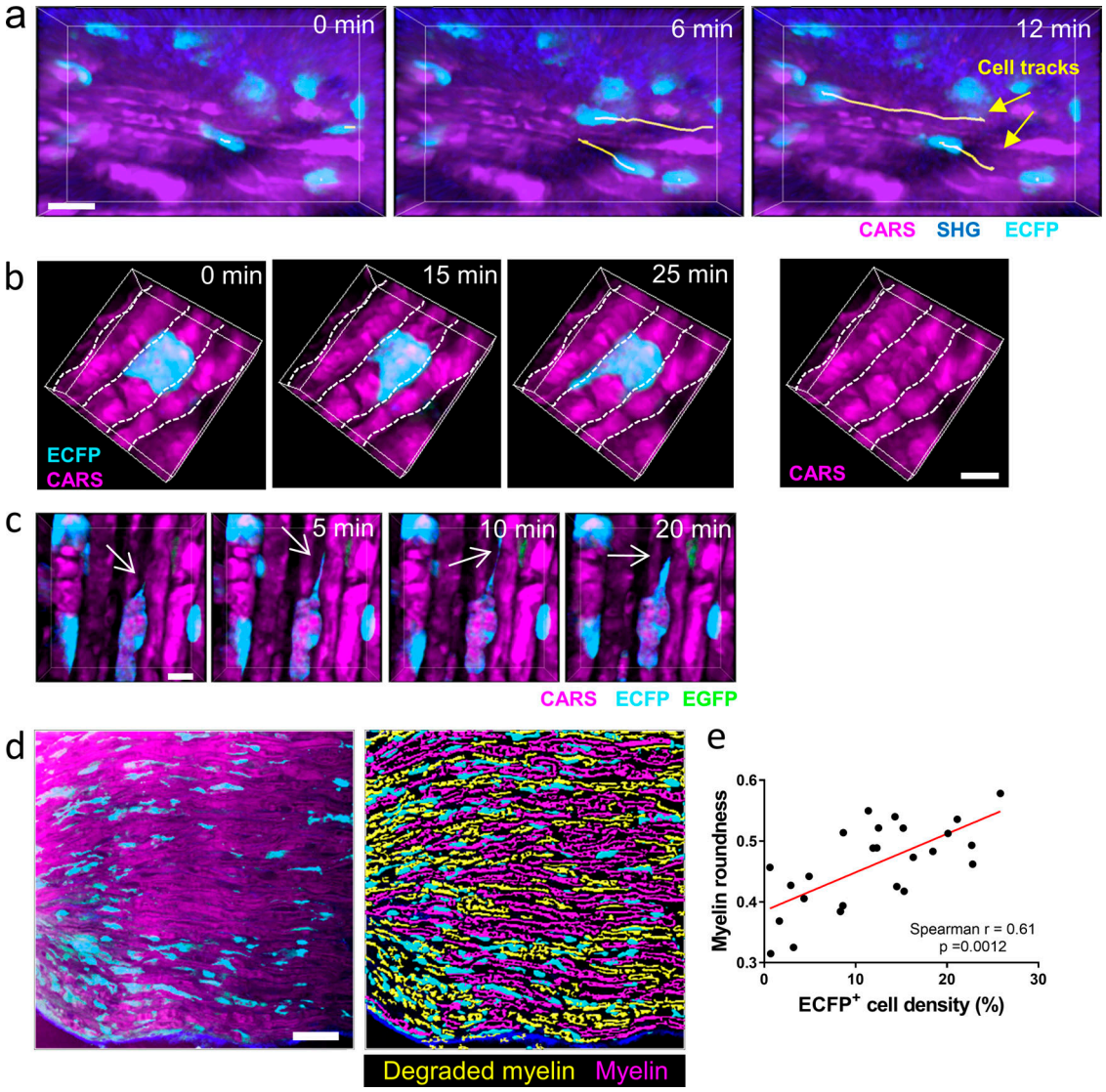


Figure S3. **Recruited MPs carry on myelin degradation and clearance. (a)** Time-lapse TPLSM 3D sequence shows ECFP⁺ cell displacement in sciatic nerve 5 d after CCI. Scale bar = 15 µm. **(b)** Time-lapse TPLSM 3D sequence shows encapsulation of the myelin sheath by ECFP⁺ cell in region of myelin breakdown. Scale bar = 10 µm. **(c)** Time-lapse TPLSM 3D sequence shows ECFP⁺ phagocytic cell extending long protrusion along myelin sheath (indicated by white arrow). Scale bar = 10 µm. **(d)** TPLSM image with 3D-masking illustrates the accumulation of ECFP⁺ cells (cyan) in region of highly degraded myelin (yellow) compared with less degraded myelin (purple). Scale bar = 50 µm. Dynamic studies are representatives of four different mice from independent experiments. **(e)** The density of ECFP⁺ cells in sciatic nerves 10 d after CCI correlates with higher myelin degradation (according to myelin roundness measurements from TPLSM 3D images). Plots represent fields collected from three different nerves processed independently.

Video 1. **Mo/MP behavior during WD of the sciatic nerve**. Time-lapse 3D imaging shows the different motions and interactions of ECFP⁺ cells (cyan) with the myelin sheath (purple) in explanted live sciatic nerve 5 d after CCI in a MacBlue × *Cx3cr1*$^{egfp/+}$ mouse. ECFP and EGFP are detected by multi-photon excitation fluorescence, and myelin is detected by CARS imaging. Video is representative of at least three mice. Speed is ×150.

Video 2. **MP stripping a myelin sheath.** Time-lapse 3D imaging shows myelin (purple) stripping by ECFP⁺ MP (cyan) in explanted live sciatic nerve 10 d after CCI in a MacBlue × *Cx3cr1*$^{egfp/+}$ mouse. ECFP and EGFP are detected by multi-photon excitation fluorescence and myelin is detected by CARS imaging. Imaging was performed. Video is representative of more than three mice. Speed is ×150.

Table S1 is provided online and lists the 124 differentially expressed genes.

Downloaded from http://rupress.org/jem/article-pdf/217/11/e20200471/1047202/jem_20200471.pdf by Curie Bib Paris user on 08 December 2020